Research Article | Vol. 10, No. 12 / 1 December 2019 / Biomedical Optics Express 6145
Biomedical Optics EXPRESS

Toward development of a large field-of-view cancer screening patch (CASP) to detect cervical intraepithelial neoplasia

JOHN GAWEDZINSKI,[1] KATHLEEN M. SCHMELER,[2] ANDREA MILBOURNE,[2] PREETHA RAMALINGAM,[3] PARNIAN A. MOGHADDAM,[4] REBECCA RICHARDS-KORTUM,[1,5] AND TOMASZ S. TKACZYK[1,5,*]

[1]*Department of Bioengineering, Rice University, 6100 Main Street, Houston, TX 77005, USA*
[2]*Departments of Gynecologic Oncology and Pathology, The University of Texas M.D. Anderson Cancer Center, 1515 Holcombe Boulevard, Houston, TX 77030, USA*
[3]*Departments of Pathology, The University of Texas M.D. Anderson Cancer Center, 1515 Holcombe Boulevard, Houston, TX 77030, USA*
[4]*Department of Pathology and Laboratory Medicine, University of Texas Health Science Center, Lyndon B Johnson Hospital, 5656 Kelley St, Houston, TX 77026, USA*
[5]*Department of Electrical and Computer Engineering, Rice University, 6100 Main Street, Houston, TX 77005, USA*
[*]*ttkaczyk@rice.edu*

Abstract: Cervical cancers are primarily diagnosed via colposcopy, in which the tissue is visually assessed by a clinician for abnormalities, followed by directed biopsies and histologic analysis of excised tissue. Optical biopsy technologies offer a less invasive method of imaging such that subcellular features can be resolved without removing tissue. These techniques, however, are limited in field-of-view by the distal end of the probe. We present a prototype that incorporates a rigid, machinable waveguide that is in direct contact with a fluorescently-labeled sample paired with a scanning fluorescent microscope. The system is capable of imaging large areas of tissue without the need to re-position the tissue-probe interface. A mosaicing algorithm was developed to quantify scanning shifts and stitch neighboring frames together to increase the field-of-view. Our prototype can yield a maximum axial resolution of <5 μm for individual frames and can produce mosaiced images with a field-of-view greater than 15 mm x 15 mm without sacrificing resolution. We validated the system with a 1951 USAF resolution target, fluorescent in vitro standards, and a patient study where *ex vivo* conization samples of squamous cervical epithelium were imaged. The results of the patient study indicate that architectural features of subcellular components could be detected and differentiated between normal tissue and precancerous lesions.

1. Introduction

In 2018, an estimated 570,000 new cases of cervical cancer were diagnosed globally [1]. Standard cervical cancer screening procedures begin with a Papanicolaou test (Pap smear) and/or human papillomavirus (HPV) DNA test performed on a sample of cells collected from the squamocolumnar junction of the cervix. If abnormalities are detected, follow-up colposcopy with biopsy of regions-of-interest is performed. Microscopic analysis of biopsies is used to identify the presence of cervical cancer and its precursor, cervical intraepithelial neoplasia (CIN). 75% of invasive cervical carcinoma begins with neoplastic lesions in the squamous epithelium along the ectocervix [2]. These neoplastic lesions can be detected by observing changes in the squamous cell nuclei including nuclear size, nuclear density, nuclear-cytoplasmic ratio (N/C ratio), and nuclear morphology [3].

#376526 https://doi.org/10.1364/BOE.10.006145
Journal © 2019 Received 28 Aug 2019; revised 24 Oct 2019; accepted 27 Oct 2019; published 6 Nov 2019

Biomedical Optics EXPRESS

The presence of a neoplastic lesion is determined by histological features of the cells themselves, while the grade of a neoplastic lesion is determined by the thickness of epithelium containing transformed cells. For mild dysplasia (CIN 1), neoplastic cells are concentrated near the basement membrane in the bottom third of the epithelial layer, while neoplastic cells appear throughout the basal 2/3 of the epithelium in moderate dysplasia (CIN 2) and the entire epithelial layer for severe dysplasia (CIN 3) [4].

There are a number of limitations associated with the current gold standard of colposcopy-directed biopsy for detection of cervical pre-cancer. First, it can take over 6 weeks between the initial cytology exam of the patient to eventually receive the biopsy results, and the number of procedures require multiple patient visits for both diagnosis and treatment [5]. Second, the specificity of colposcopy is low [6] and multiple biopsies of colposcopically-abnormal but histologically-normal areas adds to the cost of the procedure [5]. Furthermore, the procedure requires an excision of tissue for histopathological examination. Real-time imaging at the point-of-care could enable real-time, minimally-invasive detection of cervical precancer with high sensitivity and specificity, enabling combined detection and treatment in a single visit.

Endomicroscopy provides an alternative method to obtain real-time microscopic images of tissue with high resolution. High resolution imaging with microscopic probes capable of resolving subcellular components that are smaller than 10 μm [7–10]. Confocal laser microendoscopy [7], high resolution microendoscopy [8], dual mode endomicroscopy [9], and diffuse optical microscopy [10] are a few techniques that have emerged which can assess subcellular features or quantitative parameters *in vivo*. However, existing endomicroscopy techniques are limited in field-of-view (FOV) by the size of the fiber optic probe, which is typically less than 1 mm^2 [11]. The surface area of the cervical epithelium-at-risk is at least 650 mm^2, assuming the diameter of the ectocervix is 20-30 mm, and the diameter of the endocervical canal is 8 mm [12]). Thus, existing endomicroscope probes image less than 0.2% of the squamous epithelium per individual frame.

Currently, endomicroscopy probes are used in tandem with colposcopy following application of acetic acid to identify potentially suspicious areas to image [7–8]. This limits high resolution imaging only to specific sites qualitatively observed by the clinician and does not provide a full dataset across the entire field-of-interest. One method to enhance the field of view is to take subsequent neighboring images and algorithmically stitch them together in a process known as mosaicing. Previously, mosaicing algorithms have been developed for endomicroscopic technologies using a planar image stitching with correction for local surface deformations [13,14]. Mosaicing enables the creation of images that are much larger than the individual frames used to algorithmically stitch a full field-of view together, although the field-of view for individual frames remains limited by the inherent geometric restraints of the fiber bundle. Thus, performing these mosaicing techniques requires mechanical translation of the probe, which is typically in direct contact with the tissue-of-interest in microendoscopy. This approach is difficult to implement *in vivo* due to logistical complications of translating the probe across the entire tissue of interest while avoiding registration errors due to tissue deformations or loss of contact at the probe-tissue interface.

To efficiently image the cervical epithelium at and to minimize registration errors that result from scanning across a region of tissue with a single probe, we present a novel CAncer Screening Patch (CASP). The CASP system includes a customized waveguide to transmit a high resolution image of the entire field-of-view outside the patient where a distal optical system scans the entire area with high spatial resolution. This concept, presented in Fig. 1, outlines the expected appearance of a future in vivo system, while the rest of this paper describes the design and implementation of a benchtop prototype to validate the CASP imaging approach using *ex vivo* samples. The system utilizes a high-resolution waveguide that is in contact with the entire field of the tissue of interest. The optical system then scans across the desired field at the proximal

Biomedical Optics EXPRESS

surface of the waveguide. The system would require the use of a speculum to access a significant portion of the cervix similar to colposcopy imaging, but would require no manual scanning at the tissue/probe interface. The individual frames are then algorithmically reconstructed into a full-field image.

This approach addresses a number of challenges with clinical implementation of *in vivo* microscopy techniques. First, the waveguide maximizes contact at the surface of interest and minimizes tissue deformation with a high-resolution waveguide that is designed to conform to the cervical tissue. The high resolution waveguide is a polymer faceplate, composed of two machinable plastics, poly(methyl acrylate) (PMMA) and polystyrene (PS), that is processed to conform to the shape of a cervix. High resolution image transmission through the waveguide is achieved by utilizing Anderson Localization as the light-guiding principle, which has been reported previously by *Mafi et al* [15–17]. Anderson fibers can also guide light at all input facets, unlike conventional optical fibers which only guide light through core regions [17]. Additionally, the high resolution waveguide both translates the fluorescence excitation illumination to a tissue sample and guides the resulting emission to the proximal end, which is then scanned by obtaining consecutive imaging frames. This effectively reduces complications from attempting to smoothly guide a probe across an uneven surface. These frames are stitched together algorithmically using a cross-correlation algorithm that our lab has previously developed [18]. Finally, the CASP system also must not sacrifice resolution while achieving this large field imaging. The corresponding CASP image will thus be able to indicate to the clinician both the size and location of the lesion. Using this method, we capture a region of interest that encompasses the entire squamo-columnar junction and a large portion of the surrounding ectocervix while achieving a resolution capable of imaging subcellular features.

With this concept in mind, we designed a benchtop prototype detailed in the subsequent sections of this manuscript. The prototype uses a high-resolution waveguide that is mounted to an optical breadboard and is placed in direct contact with specimens to be imaged. The microscope uses commercially available optical components and takes a series of snapshots at the output of the waveguide to reconstruct a large-field image of the sample.

2. Methods

2.1. Assembly of fluorescence microscope

A wide-field epi-fluorescence microscope was assembled using off-the-shelf components to scan across the proximal end of the fiber optic faceplate. Table 1 lists the design specifications for the entire Cancer Screening Patch (CASP) system. Proflavine was selected as a fluorescent dye to be used for staining cell nuclei. Proflavine has an excitation peak at 443 nm and an emission peak at 511 nm [19]. A commercial 4x objective with an object space NA of 0.13 was chosen to ensure that lateral resolution is limited by what is achievable on the high-resolution waveguide detailed in Section 2.3. An object space NA of at least 0.086 for the imaging system would need to be used in order to ensure that the resolution limits of the system are determined by the waveguide.

The schematic and assembly of the CASP system are shown in Fig. 2. The proximal end of the faceplate is illuminated by a 455 nm LED (M455L2, Thorlabs Inc., Newton, New Jersey) in a Koehler illumination setup. The resulting illumination intensity at the proximal end of the faceplate was measured as 3.24 mW/cm^2. The emission is captured on the proximal end through a 4x 0.13 NA commercial objective (UPlanFI, Olympus Corp., Tokyo, Japan) and passes through a dichroic filter and long-pass emission filter. A compatible tube lens (Olympus Corp., Tokyo, Japan) focuses the image onto a 1.3 MP CCD camera (GS3-U3-14S5M-C, FLIR, Wilsonville, OR). A description of the high-resolution waveguide used for biological imaging can be found in Section 2.3.

The microscope apparatus is mounted on two linear stages that scan the proximal surface of the faceplate to capture different fields-of-view. While there is a translational offset between

Biomedical Optics EXPRESS

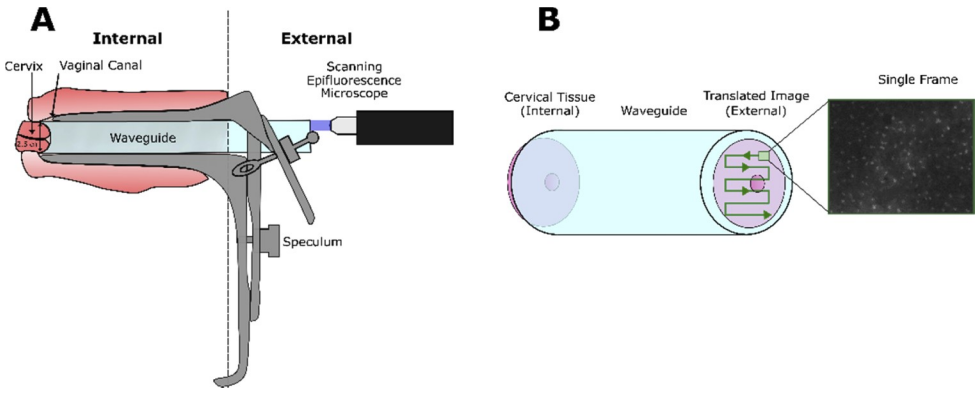

Fig. 1. Conceptual probe-tissue interface of the CASP system. (A) A custom-designed waveguide is in contact with the tissue of interest. The waveguide translates the image of the epithelial tissue to the proximal end as detailed in (B) to an area outside of the vaginal cavity, where individual frames are scanned and reconstructed into a full image.

Table 1. Application Requirements and Specifications for Imaging Optics

Excitation Wavelength	411.25-464.5 nm
Emission Wavelength	483.5-565 nm
Waveguide Resolution	4 µm
Minimum Object Space NA required for optics	0.086
Imaging System Resolution	2.65 µm
Object Space NA of Imaging System	0.13
Single-Frame Field-of-View (diameter)	1 mm
Total Field-of-View (diameter)	15 mm

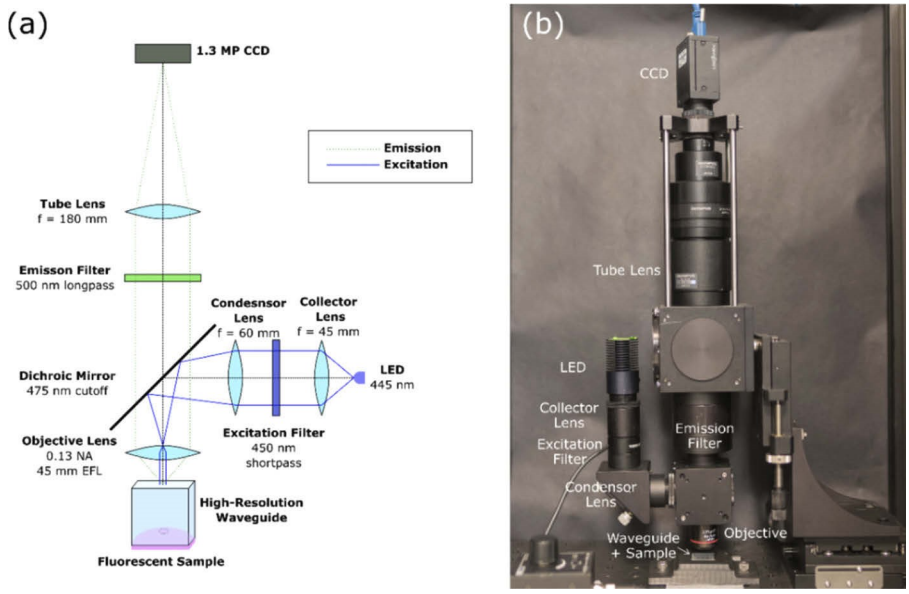

Fig. 2. (A) Design of epi-fluorescence scanning microscope. (B) Assembled CASP system.

Biomedical Optics EXPRESS

consecutive frames, there is a sizeable area of overlap for full image reconstruction purposes described in the mosaicing algorithm section below. The faceplate and sample are independently fixed to the breadboard with a custom 3D-printed mount.

2.2. High-resolution fiber optic waveguide

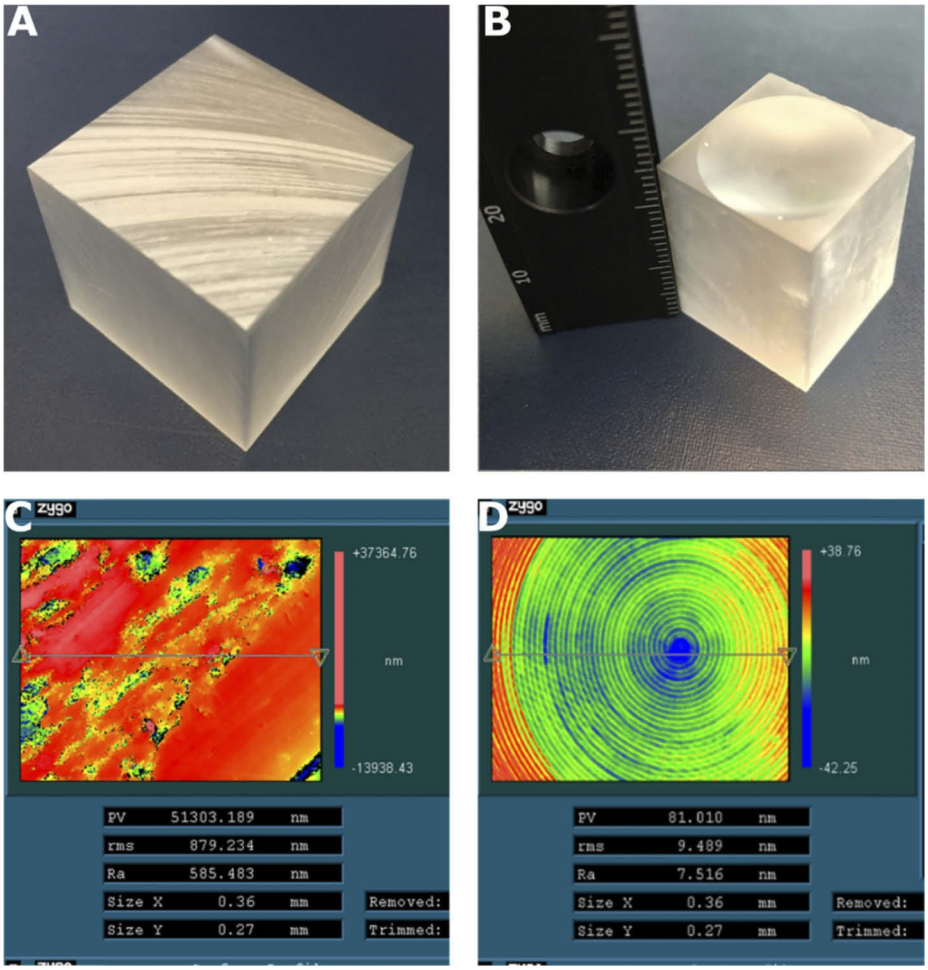

Fig. 3. Machining process of Fiber Optic Faceplate. (A) is the faceplate prior to any machining where (C) represents the initial surface profile obtained using white-light interferometry. (B) represents the faceplate after the final cut with a ruler for scale, while (D) shows the improvement in surface quality after machining.

Unpolished samples of a commercially-available high-resolution polymer faceplate were obtained from Incom (Incom Inc., Charlton, MA, USA). The Incom Nanoguide [20] waveguides used for biological imaging were initially 20 mm × 20 mm on the transverse plane and 25.4 mm (1") thick as a proof-of-concept design. The faceplate is mechanically rigid and contains a 50/50 mix of strands of polystyrene (PS) and poly methyl methacrylate (PMMA) distributed stochastically across the transverse plane. Strands are compacted into preforms and drawn into Anderson waveguiding fibers as detailed by Mafi et al [16]. A larger assembly of several Anderson cores is performed to manufacture the image guides. PS has a refractive index of 1.59, while PMMA has a refractive index of 1.49. The strands are deposited such that the transverse

Biomedical Optics EXPRESS

plane has a random pattern of polystyrene and PMMA input fiber locations, but the refractive index across the longitudinal plane is fixed. The numerical aperture of the waveguide is 0.85.

Samples were then custom-machined using an in-house single point diamond turning lathe. First, flat cuts were made to polish the distal and proximal surfaces to a roughness of optical quality (<10 nm). Afterwards, a dome shape was cut into the distal end of the faceplates to both adhere to an *in vivo* cervical model, while also allowing us to maximize contact between the faceplate and the tissue for *ex vivo* samples. The dome was cut with a radius of curvature of 25 mm with a 5 mm depth of cut. Figure 3 shows the product both pre-and-post-processing with corresponding white light interferometry measurements to highlight the change in surface roughness. Peak-to-valley, root mean squared, and arithmetic average of the absolute values (Ra) of the surface were used to assess the roughness. Samples used to test resolution of a 1951 USAF resolution test chart (Section 3.1) were polished flat on both sides to achieve uniform contact with the target.

2.3. Mosaicing algorithm

After a sequence of images across the field-of-view has been taken, frames are algorithmically stitched together to create a full-field image. We use a fast registration algorithm reported in [21], where the cross-correlation between consecutive frames is calculated with their discrete Fourier transforms (DFTs). Here, translational offset between neighboring frames f(x,y) and g(x,y) are calculated using the following equation:

$$r_{fg}(x_i, y_i) = \sum_{u,v} F(u,v)G^*(u,v) \exp\left[i2\pi\left(\frac{ux_i}{M} + \frac{vy_i}{N}\right)\right] \quad (1)$$

where F and G represent the DFTs, * designates the complex conjugate, and M and N symbolize the dimensions of the image. The inverse FFT of the product is used to determine the cross-correlation, where the calculated lateral shift is determined by the location of the peak value of the cross-correlation. A registration matrix is generated that reports the lateral shifts for each frame from the frame previously calculated. For reconstruction, the first frame is copied to a zero-value canvas, and subsequent frames are inserted into the image in sequence based on the registration matrix. For overlapping pixels between new frames and the current mosaic, the maximum value found is used.

To avoid motion blurring, stages were translated at a speed of ~1.0 mm/s during acquisition. An overlap of ~70% was also done between consecutive images to minimize registration error. Another significant source of error can be found in areas with high levels of low-spatial-frequency information (such as very dark or very bright areas). To account for these, twenty local maxima for each cross correlation calculation were recorded. The local maxima which produced the smallest normalized root-mean-square error for the corresponding overlapping regions was registered as the correct shift.

3. Results

3.1. System performance

The lateral resolution of the CASP was assessed using a 1951 USAF resolution test targets. A white light LED (MBB1L3, ThorLabs, USA) was coupled to a Köhler illumination system that irradiated the test target. First, we evaluated the performance of the assembled imaging microscope alone with no image guide used on a high-resolution target. We then evaluated the system using two separate image guides for comparison. The results are presented in Fig. 4. In Fig. 4(b), the assembled microscope coupled to a commercially-available high-resolution 790-µm-diameter multimodal optical fiber bundle with 4.4-µm core-to-core spacing. We then exchanged the fiber bundle with a 25.4 mm thick sample of the high-resolution faceplate that was cut flat on both the distal and proximal ends, which is presented in Fig. 4(c). The fiber bundle

Biomedical Optics EXPRESS

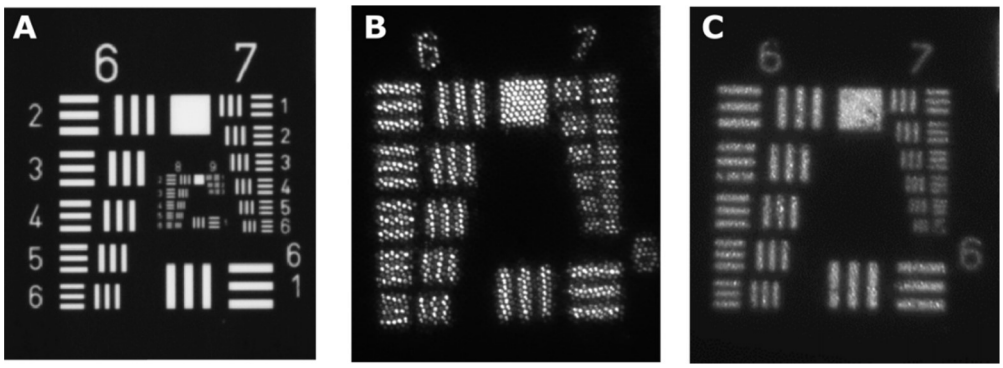

Fig. 4. Images of USAF targets taken with the CASP epifluorescence microscope illuminated with a white LED. In (A) no image guide is used. In (B) the microscope is coupled to a static fiber bundle with 4.4 μm core-to-core spacing, while (C) shows the performance of the system using the high-resolution waveguide.

should have a theoretical resolution limit of 8.8 μm due to Nyquist criteria, corresponding to a resolution limit of around Group 6 element 6. As shown in Fig. 7(b), the microscope coupled to the fiber bundle is capable of resolving up to Group 6, Element 6 (114.0 lp/mm) but does not discernably resolve any smaller features. The system using the Anderson Faceplate has a theoretical resolution of about 4 μm as provided by the manufacturer [20]. This would correspond with the ability to be able to resolve just beyond Group 7, Element 6 for a white light illumination source. As shown in Fig. 7(c) can achieve a resolution of Group 7, Element 5 (203.2 lp/mm), in our epifluorescence microscope. As the bandwidth of light used for this experiment was limited to only wavelengths above our emission filter cutoff, we can expect to see some small difference in the resolution reported by the manufacturer and our experiment, as wavelength is an independent variable that affects the localization beam width for Anderson waveguides [17]. Other applications of this technology using shorter wavelengths could result in a slightly improved resolution.

The fluorescence imaging and mosaicing capabilities of the system were evaluated using a fluorescently-labeled sample of lens paper, stained with proflavine dye. We acquired a 20 mm x 4 mm field-of-view of the lens paper and mosaiced 300 frames with ~75% overlap to generate our large-field image displayed in Fig. 5. Registration worked optimally with a maximum speed of ~1.35 mm/s with a frame rate of 8 FPS. The mosaic algorithm successfully stitched the frames together with minimal artifacts due to registration error. Spatial features additionally maintain their size and morphology.

3.2. Clinical study of ex vivo cervical tissue

To evaluate the potential of the device to differentiate between normal and precancerous cervical epithelium, cervical conization specimens were imaged directly after excision. Eighteen patients gave consent for a study that was approved by the Institutional Review Boards (IRBs) at Rice University and MD Anderson Cancer Center in partnership with Lyndon B Johnson Hospital in Houston, TX. The participants underwent a standard of care loop electrosurgical excision procedure (LEEP) for treatment of cervical precancer, in which a ~1 cm diameter disc was cut around the squamo-columnar junction of the cervix with a thickness of ~8 mm with +/- 4 mm of variance in the thickness of the samples. After removal, the ex vivo tissue was stained with a 0.02% w/v proflavine solution (Sigma Aldrich, St. Louis, Missouri) in 1X PBS and imaged under the CASP system. After imaging, tissue samples were sent to the pathologist to be prepared for routine histopathological examination per standard of care. Regions of the

Biomedical Optics EXPRESS

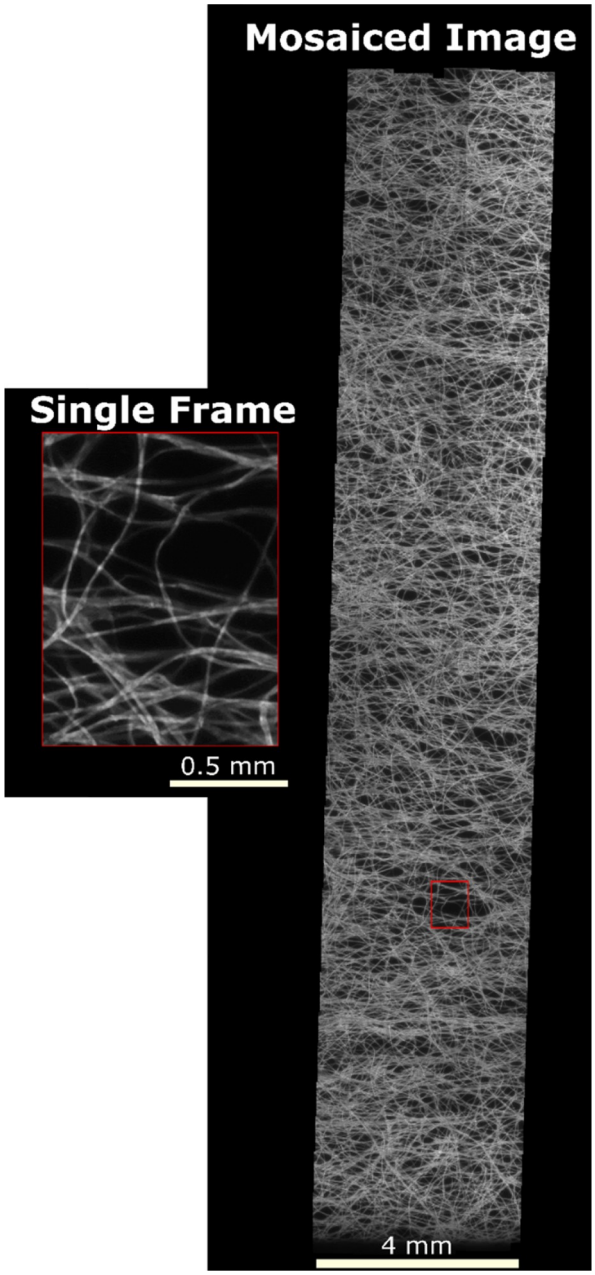

Fig. 5. Mosiac image of fluorescently-labeled lens paper. The boxed region represents a single frame taken in the image sequence, while the mosaiced image shows a full 20 mm x 4 mm FOV of neighboring frames.

Biomedical Optics EXPRESS

squamocolumnar junction were subsequently evaluated by the pathologist. All specimens were classified by the level of CIN found in the epithelial tissue examined. Samples were classified as no neoplasia, low-grade cervical intraepithelial neoplasia (CIN 1) or high-grade cervical intraepithelial neoplasia (CIN 2/3), with the location of precancerous lesions indicated.

The samples were secured to the optical table in direct contact with the distal end of a machined faceplate sample. The sample was evaluated at several different locations across the region-of-interest to determine whether contact was made across a significant field-of-view. Six of the eighteen samples were geometrically incompatible with the machined faceplates, as they were not thick enough along all points along the ectocervical epithelium in the sample to make contact over a significant area-of-interest. This form of geometric incompatibility was independent to this ex vivo study, as it relied on the sample confirming to a pre-machined image guide used for the study. Thickness will not be a limiting factor for future in vivo studies of intact cervical tissue, and future ex vivo studies incorporate more waveguide geometries to maximize contact along the sample. The remaining 12 samples were imaged and mosaiced. Table 2 summarizes the patient samples that were imaged and evaluated by the CASP system. The table has been organized to group patients with similar diagnoses together. Figure 6 displays the imaging process for one patient with low-grade neoplasia.

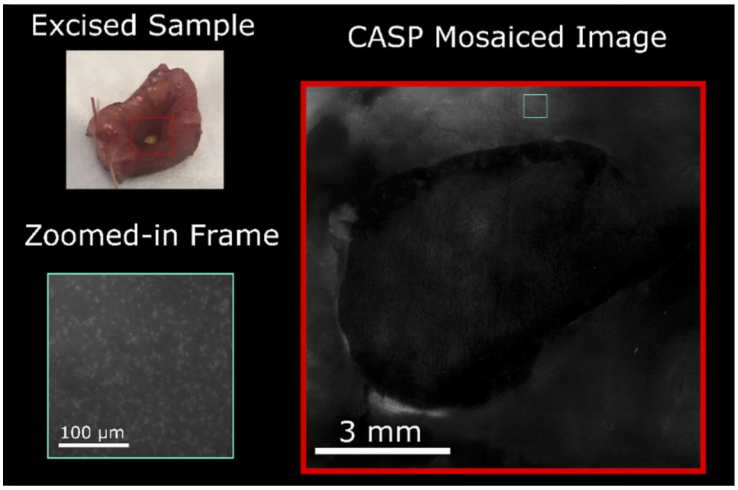

Fig. 6. Mosaiced image of *ex vivo* tissue with low-grade neoplasia. The excised sample is shown in the top left. The full mosaiced image is presented on the right, and the bottom left highlights a zoomed-in region to display the resolution of the system. The fluorescently-labeled features are nuclei in the squamous epithelium of the cervical tissue.

Table 2. Summary of histopathological diagnoses for clinical trial

Diagnosis	Description	Total Patients Imaged (n = 12)	% of Imaged Patients
No neoplasia	No abnormalities	2	16.7%
CIN 1	Abnormalities in bottom third of squamous epithelium.	3	25%
CIN 2/3	Neoplastic cells between bottom 2/3 of epithelium to the external surface.	7	58.3%

Biomedical Optics EXPRESS

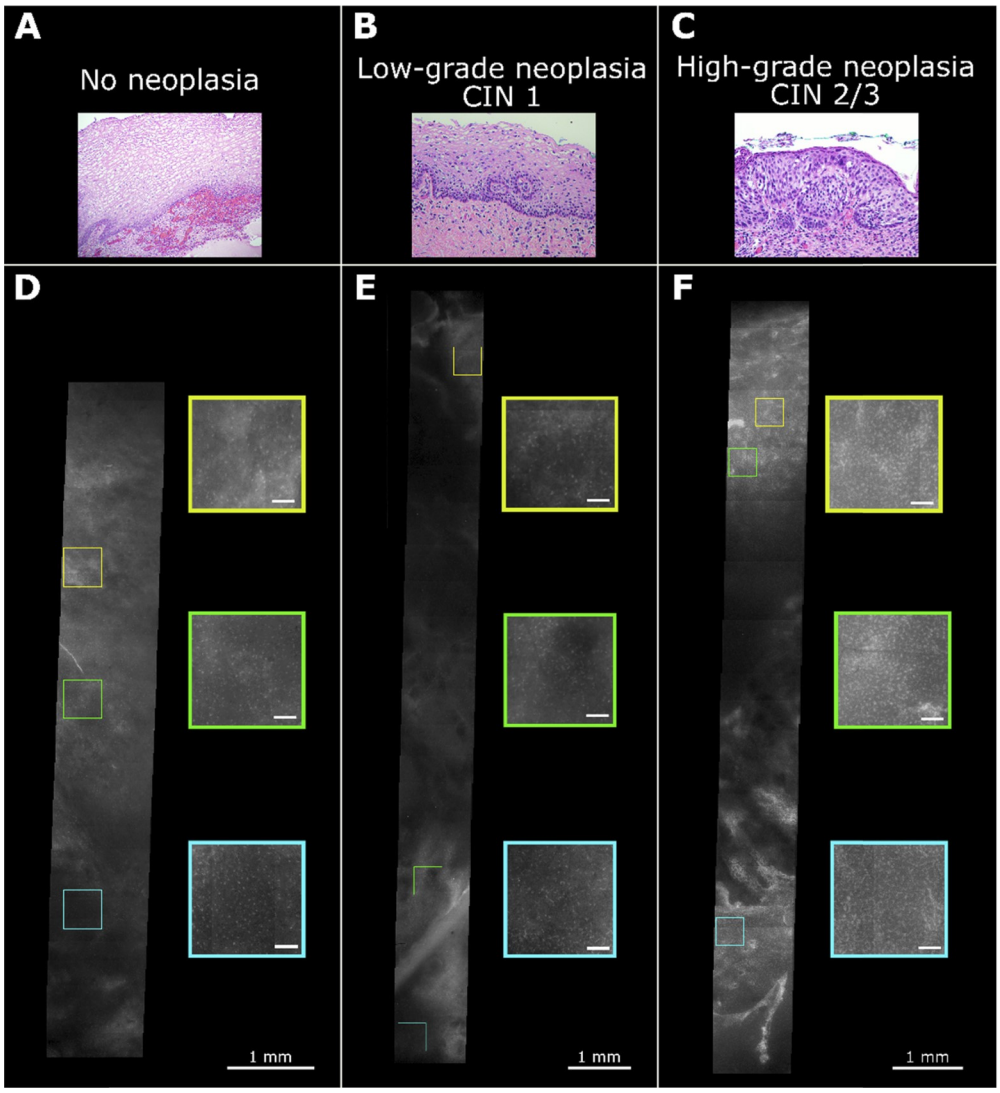

Fig. 7. (A) Histopathology of a patient with no neoplasia found. A CASP mosaic of a region of this sample's tissue is shown in (D). (B) Histopathology of a patient with low-grade cervical intraepithelial neoplasia, with (E) a corresponding CASP image. (C) and (F) Histopathology and CASP image of patient with high-grade cervical intraepithelial neoplasia. Magnified FOVs are highlighted for each CASP image to highlight the much larger N/C ratio seen in high-grade neoplasia. Scale bars for highlighted regions are 100 µm.

Biomedical Optics EXPRESS

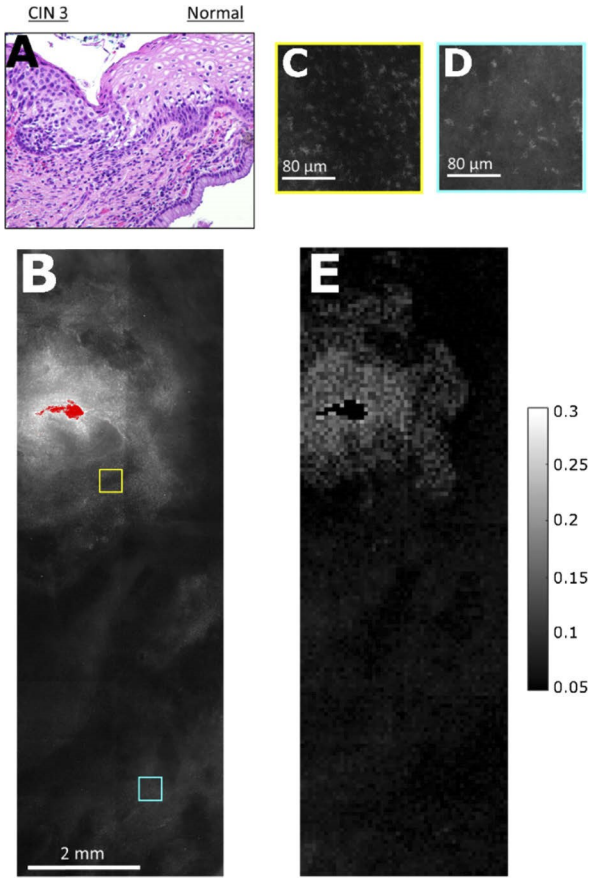

Fig. 8. Histology map used to threshold for detection of abnormalities in patient data. (A) Pathology map of the junction between a detected lesion and the surrounding healthy tissue, while (B) is the corresponding CASP image of the area of the cervix the lesion was detected. (C) Magnified view of nuclei at the threshold of the lesion, while (D) displays nuclei outside the lesion. (E) is a map of measured nuclear-to-cytoplasmic ratio for calculated from the CASP image

The mosaic in Fig. 6 shows that we can image across tissue samples that are 1 cm in diameter while still being able to observe subcellular features. By zooming in at particular regions-of-interest in the larger mosaiced image, we can then begin to assess nuclear features. We decided to evaluate N/C ratio, which has been previously validated as a metric for evaluation of precancer in cervical tissue [8,22–23]. Figure 7 shows an observation of different nuclear to cytoplasmic ratios seen in patients with different diagnoses.

As seen in the pathology images in Fig. 7(a-c), the concentration and shape of nuclei in the squamous epithelium increases as the stage of precancer progresses. Similarly, regions imaged by the CASP system on the same samples shown in Fig. 7(d-e) highlight that a similar trend can be seen in these images, as the morphology and density of nuclei raises dramatically between absent and low-grade neoplastic tissue as compared to the lesion sites that are imaged within the sample of a patient with a high-grade neoplasia.

To evaluate whether or not the system could identify specific abnormalities found within a full mosaiced image, we created a histological map based on a patient with a known location of a precancerous lesion. An image was captured that displayed both the lesion and the surrounding

Biomedical Optics EXPRESS

healthy tissue. Figure 8 displays the pathology image where the junction between the lesion and the surrounding healthy tissue is shown. Nuclear-to-cytoplasmic ratio was calculated by separating the nuclei from the background and counting the number of pixels found to be part of the nuclei as compared to the surrounding background. To do this, the CASP image in Fig. 8 was sectioned into overlapping 200 µm × 200 µm fields-of view. For each field of view, the location of each nucleus was identified manually and input into a custom MATLAB program. Adaptive thresholding was performed at these locations to effectively binarize the image and separate each nucleus from the corresponding background. For each pixel, all neighboring pixels within a 41 pixel x 41 pixel radius are analyzed. If the pixel if found to be above the local mean intensity, it is determined to be part of the foreground and becomes a white pixel. If not, the pixel is colored black and considered part of the background. The N/C ratio of the corresponding field-of-view was calculated by counting the number of white pixels in the image, which corresponded to nuclei. Translational overlap between measured fields-of-view was 25 pixels. Figure 8E displays the final results in which each pixel represents the average calculated N/C ratio for each field-of-view that overlapped that specific 25 pixel × 25 pixel area. At the junction of the lesion and the surrounding healthy tissue, the average measured N/C ratio was measured to be 0.135. Previous studies have indicated that the measured N/C ratio is significant when it is greater than 0.16 [8].

We then selected twenty 200 µm × 200 µm sites for each CASP image and calculated the N/C ratio at each site. When N/C ratio measured above the 0.135 threshold determined by our histology map, the site was flagged as "abnormal." Figure 9 displays the graph summarizing the measurements for each region. All twenty sites for the five patients who had either no neoplasia or CIN 1 reported in their pathology diagnosis were found to be below the 0.135 N/C ratio. Additionally, each of the patients with high-grade neoplasia had at least one site that was flagged as "abnormal," while one patient did not have a single site that measured below the threshold.

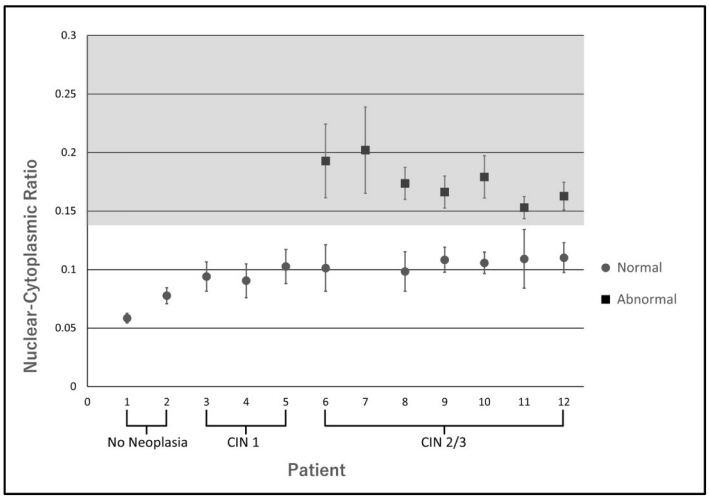

Fig. 9. N/C ratio calculated at 20 sites for each tissue sample. Sites that had N/C ratio above 0.135 were flagged as abnormal and are displayed in the gray region and were only found in patients with high-grade neoplasia. Sites that were measured below the threshold were found in all samples except one patient with high-grade neoplasia. Error bars showing the standard deviation for all normal and abnormal sites are displayed for each dataset.

Biomedical Optics EXPRESS

4. Discussion and conclusions

An imaging system was designed for the identification of precancerous lesions in cervical tissue across a large field-of-view. The device was validated using a 1951 USAF resolution target, lens paper, and ex vivo samples of cervical tissue. The 1951 USAF resolution chart image presented in Fig. 4 indicates that the high resolution polymer faceplate is capable of image guiding properties with a better resolution than a 4.5 μm core-to-core fiber bundle. While the fiber bundle can only resolve up to Group 7, Element 1 (128.0 lp/mm), the Anderson faceplate can guide with a resolution of Group 7, Element 5 (203.2 lp/mm). Given that identical fiber bundles have been previously used for imaging nuclei in microendoscopic devices, this result indicates that this faceplate should be a suitable waveguide for this application. Furthermore, the faceplate is rigid and machinable as shown in Fig. 3. We were able to process the polymer faceplate to an optical quality with a roughness of under 10 nm with a custom geometry more suitable for *in vivo* cervical imaging. Preliminary work has been done to characterize light loss for these Anderson waveguides as we begin machining faceplates with dimensions suitable for scanning in a clinical setting. We evaluated samples of both 12.7 mm and 25.4 mm thicknesses and measured throughput of a 632.8 nm He-Ne laser. A photodiode power sensor was used to measure optical power of the laser at the input location along the distal end of the waveguide sample and the output location at the corresponding location along the proximal end. Measurements were taken for three samples of each thickness at five different input locations along the transverse plane of the waveguide. We observed a loss of 0.4 dB/cm. These results are preliminary, however, as they only detail measurements taken at two thicknesses. We will include further characterization in our future work as we machine more samples. This includes characterization of image guides that are up to 17 cm in length with various geometries used for the distal end of the probes.

We also incorporated a scanning system with a custom mosaicing algorithm that handles registration of neighboring frames. Both lens paper imaging and *ex vivo* tissue samples provided promising results for the algorithm to handle both high spatial frequency regions with many fluorescent objects and low-frequency regions with fewer fluorescent objects. While signal from the fluorescent dye used decreased slightly over the duration of the scan, there were no substantial photo bleaching effects observed under these conditions. We successfully stitched together scanning areas that can cover a distance of 15 mm in either axial direction. With the image guiding faceplate remaining in steady contact with the tissue, scan time is inherently limited by the field-of-view of the scanning microscope whose components can be interchanged as long as the axial resolution of the microscope does not decrease to under 203.2 lp/mm. By incorporating a higher megapixel camera sensor or potentially optical components with larger apertures, the field of view of individual frames could be increased and reduce scan time.

A patient study was performed which evaluated the detection abilities of the system on 12 patients with various CIN diagnoses. As shown in Fig. 7, patients that were diagnosed with an absence of any neoplastic lesions were found to have nuclei that were sparse and smaller, while patients with severe dysplasia were found to have more regions with densely populated nuclei that were larger in size. We created a histological map of a region with a neoplastic lesion and surrounding healthy tissue to create a threshold to guide evaluation of other tissue samples. We used N/C ratio as a metric to threshold for the identification of precancerous lesions and observed that patients with moderate-to-high grade dysplasia were all found to have areas in their entire field-of-view with N/C ratios that were greater than the threshold determined by the histological map. The map site was imaged by our CASP system, and we calculated N/C values at the junction between the location of the lesion and the surrounding healthy tissue. The averaged values at that junction gave us our threshold of 0.135. We then used that threshold to analyze our data from other patients to see if we detected sites that were above that threshold in the patients with high-grade intraepithelial neoplasia. We found that all patients in our 12 patient study with high-grade intraepithelial neoplasia had multiple sites along the analyzed tissue with

Biomedical Optics EXPRESS

values above that threshold. However, a larger sample of patient data with more quantitative analysis of nuclear features such as size and geometry would be required to provide the data necessary for real-time analysis required for diagnosis. For this study, there was a clear distinction in N/C ratio for patients with nonexistent to low grade dysplasia as compared to patients with high-grade dysplasia that carries a much more significant risk. This suggests the system could be promising as a method for specifically identifying high-grade neoplastic lesions with a high specificity. Additionally, proflavine was used to stain and image the nuclei in the tissue sample. While clinical use of proflavine has been long-standing, some recent studies have evaluated whether exposure to proflavine can increase cervical cancer risk and found no differences in rates of neoplastic progression in patients exposed to proflavine compared to comparable controls [24]. Proflavine represents one dye or contrast agent that could be used with this technology. Alternatives such as methylene blue [25] or fluorescein [26] could be substituted with only minor changes to the optical filters and illumination bandwidth used in the design.

By using a custom-machined, high resolution fiber optic faceplate in contact with the tissue of interest, we can construct large-field images of fluorescently-labeled subcellular features without moving any components inside the patient cavity. The polymer faceplate is more customizable than commercially available fiber optic products and can guide light coupled at any location at the input, as compared to traditional fiber optics which do not couple light at cladding interfaces. Future work will involve miniaturizing the optical system and fabricating faceplates that can be used for integrated ex vivo and in vivo clinical studies using a concept similar to what was presented in Fig. 1. To address the issue with geometrical compatibility of samples we imaged in this paper, we will be fabricating more CASP image guide geometries with various curvatures and depth of cuts to accommodate the different samples we might encounter. Furthermore, the faceplate will need to be packaged to make the procedure as minimally invasive as possible, fitting within geometric constraints for typical colposcopy procedures. The optical scanning system will have to be designed such that all movement happens outside of the patient, but must be as ergonomic and light as possible. Additionally, contrast enhancement techniques could potentially be applied to the simple optics of the current system to improve signal-to-noise ratio in the corresponding images. These *in vivo* studies can evaluate the device as an ancillary tool for evaluation of neoplastic cervical tissue across a large FOV.

Funding

National Cancer Institute (CA209063).

Disclosures

Dr. Tomasz Tkaczyk has financial interests in Attoris LLC focusing on applications and commercialization of hyperspectral imaging technologies.

References

1. . International Agency for Research on Cancer, "Cervix uteri," https://gco.iarc.fr/today/data/factsheets/cancers/23-Cervix-uteri-fact-sheet.pdf. Accessed: 7-Mar-2019.
2. L. T. Chuang, S. Temin, R. Camacho, A. Dueñas-Gonzalez, S. Feldman, M. Gultekin, V. Gupta, S. Horton, G. Jacob, E. A. Kidd, and K. Lishimpi, "Management and care of women with invasive cervical cancer: American Society of Clinical Oncology resource-stratified clinical practice guideline," Journal of Global Oncology **2**(5), 311–340 (2016).
3. J. P. Baak, A. J. Krushe, S. J. Robboy, E. A. Janssen, B. van Dierman, and I. Skaland, "Dynamic behavioural interpretation of cervical intraepithelial neoplasia with molecular markers," J. Clin. Pathol. **59**(10), 1017–1028 (2006).
4. J. W. Sellors and R. Sankaranarayanan, *Colposcopy and Treatment of Cervical Intraepithelial Neoplasia: A Beginner's Manual*. (Diamond Pocket Books Ltd., 2003).
5. B. Hill, S. F. Lam, P. Lane, C. MacAulay, L. Fradkin, and M. Follen, "Established and emerging optical technologies for the real-time detection of cervical neoplasia: a review," J. Cancer Ther. **08**(13), 1241–1278 (2017).

Biomedical Optics EXPRESS

6. S. B. Cantor, M. Cardenas-Turanzas, D. D. Cox, E. N. Atkinson, G. M. Norgueras-Gonzalez, J. R. Beck, M. Follen, and J. L. Benedet, "Accuracy of colposcopy in the diagnostic compared with the screening setting," Obstet. Gynecol. **111**(1), 7–14 (2008).
7. J. Tan, M. A. Quinn, J. M. Pyman, P. M. Delaney, and W. J. McLaren, "Detection of cervical intraepithelial neoplasia in vivo using confocal endomicroscopy," BJOG: An International Journal of Obstetrics & Gynaecology **116**(12), 1663–1670 (2009).
8. M. K. Quinn, T. C. Bubi, M. C. Pierce, M. K. Kayembe, D. Ramogola-Masire, and R. Richards-Kortum, "High-resolution microendoscopy for the detection of cervical neoplasia in low-resource settings," PLoS One **7**(9), e44924 (2012).
9. N. Bodenschatz, C. F. Poh, S. Lam, P. M. Lane, M. Guillaud, and C. E. MacAulay, "Dual-mode endomicroscopy for detection of epithelial dysplasia in the mouth: a descriptive pilot study," J. Biomed. Opt. **22**(08), 1 (2017).
10. N. Bodenschatz, S. Lam, A. Carraro, J. Korbelik, D. M. Miller, J. N. McAlpine, M. Lee, A. Kienle, and C. E. MacAulay, "Diffuse optical microscopy for quantification of depth-dependent epithelial backscattering in the cervix," J. Biomed. Opt. **21**(6), 066001 (2016).
11. J. S. Louie, R. Richards-Kortum, and S. Anandasbapathy, "Applications and advancements in the use of high-resolution microendoscopy for detection of gastrointestinal neoplasia," Clin. Gastroenterol. Hepatol. **12**(11), 1789–1792 (2014).
12. R. J. Kurman, *Blaustein's Pathology of the Female Genital Tract* (4th ed.). (Springer, 1994) pg. 185–204.
13. T. Vercauteren, A. Perchant, G. Malandain, X. Pennec, and N. Ayache, "Robust mosaicing with correction of motion distortions and tissue deformations for in vivo fibered microscopy," Med. Image Anal. **10**(5), 673–692 (2006).
14. K. E. Loewke, D. B. Camarillo, W. Piyawattanametha, M. J. Mandella, C. H. Contag, S. Thrun, and J. K. Salisbury, "In vivo micro-image mosaicing," IEEE Trans. Biomed. Eng. **58**(1), 159–171 (2011).
15. H. De Raedt, A. D. Lagendijk, and P. de Vries, "Transverse localization of light," Phys. Rev. Lett. **62**(1), 47–50 (1989).
16. S. Karbasi, R. J. Frazier, K. W. Koch, T. Hawkins, J. Ballato, and A. Mafi, "Image transport through a disordered optical fibre mediated by transverse Anderson localization," Nat. Commun. **5**(1), 3362 (2014).
17. S. Karbasi, C. R. Mirr, P. G. Yarandi, R. J. Frazier, K. W. Koch, and A. Mafi, "Observation of transverse Anderson localization in an optical fiber," Opt. Lett. **37**(12), 2304–2306 (2012).
18. N. Bedard, T. Quang, K. Schmeler, R. Richards-Kortum, and T. S. Tkaczyk, "Real-time video mosaicing with a high-resolution microendoscope," Biomed. Opt. Express **3**(10), 2428–2435 (2012).
19. Oregon Medical Laser Center, "Proflavin," https://omlc.org/spectra/PhotochemCAD/html/078.html. Accessed: 7-Mar-2019.
20. Incom, Incorporated. "Nanoguide™," https://incomusa.com/wp-content/uploads/Nanoguide-New-format-Final.pdf. Accessed: 7-Mar-2019.
21. M. Guizar-Sicairos, S. T. Thurman, and J. R. Fienup, "Efficient subpixel image registration algorithms," Opt. Lett. **33**(2), 156–158 (2008).
22. K. B. Sung, R. Richards-Kortum, M. Follen, A. Malpica, C. Liang, and M. R. Descour, "Fiber optic confocal reflectance microscopy: a new real-time technique to view nuclear morphology in cervical squamous epithelium in vivo," Opt. Express **11**(24), 3171–3181 (2003).
23. N. Benzerdjeb, C. Garbar, P. Camparo, and H. Sevestre, "Digital holographic microscopy as screening tool for cervical cancer preliminary study," Cancer cytopathology **124**(8), 573–580 (2016).
24. N. Pantano, B. Hunt, R. A. Schwarz, S. Parra, K. Cherry, J. C. Possati-Resende, A. Longatto-Filho, J. H. T. G. Fregnani, P. E. Castle, K. Schmeler, and R. Richards-Kortum, "Is proflavine exposure associated with disease progression in women with cervical dysplasia? A brief report," Photochem. Photobiol. **94**(6), 1308–1313 (2018).
25. B. Obstoy, M. Salaun, L. Veresezan, R. Sesboüé, P. Bohn, F. X. Boland, and L. Thiberville, "Safety and performance analysis of acriflavine and methylene blue for in vivo imaging of precancerous lesions using fibered confocal fluorescence microscopy (FCFM): an experimental study," BMC Pulm. Med. **15**(1), 30 (2015).
26. S. P. Prieto, K. K. Lai, J. A. Laryea, J. S. Mizell, W. C. Mustain, and T. J. Muldoon, "Fluorescein as a topical fluorescent contrast agent for quantitative microendoscopic inspection of colorectal epithelium," Biomed. Opt. Express **8**(4), 2324–2338 (2017).